An Earth-sized Planet around an M5 Dwarf Star at 22 pc

N.B. When citing this work, cite the original published paper.

(article starts on next page)

An Earth-sized Planet around an M5 Dwarf Star at 22 pc

Teruyuki Hirano[1,2,3], Fei Dai[4,5,6], John H. Livingston[1,2,3], Sascha Grziwa[7], Kristine W. F. Lam[8], Yui Kasagi[2,3],
Norio Narita[1,9,10], Hiroyuki Tako Ishikawa[1,2], Kohei Miyakawa[2], Luisa M. Serrano[11], Yuji Matsumoto[2],
Eiichiro Kokubo[2], Tadahiro Kimura[12], Masahiro Ikoma[2,12], Joshua N. Winn[13], John P. Wisniewski[14],
Hiroki Harakawa[15], Huan-Yu Teng[16], William D. Cochran[17], Akihiko Fukui[9,10], Davide Gandolfi[11],
Eike W. Guenther[18], Yasunori Hori[1,2,3], Kai Ikuta[19], Kiyoe Kawauchi[19], Emil Knudstrup[20], Judith Korth[21],
Takayuki Kotani[1,2,3], Vigneshwaran Krishnamurthy[1,2], Tomoyuki Kudo[15], Takashi Kurokawa[1,22], Masayuki Kuzuhara[1,2],
Rafael Luque[23], Mayuko Mori[24], Jun Nishikawa[1,2,3], Masashi Omiya[1,2], Jaume Orell-Miquel[25,26], Enric Palle[25,26],
Carina M. Persson[27], Seth Redfield[28], Eugene Serabyn[29], Alexis M. S. Smith[30], Aoi Takahashi[1,2], Takuya Takarada[1,2],
Akitoshi Ueda[2], Vincent Van Eylen[31], Sébastien Vievard[1,15], Motohide Tamura[1,2,24], and Bun'ei Sato[16]

[1] Astrobiology Center, 2-21-1 Osawa, Mitaka, Tokyo 181–8588, Japan; hd17156b@gmail.com
[2] National Astronomical Observatory of Japan, 2-21-1 Osawa, Mitaka, Tokyo 181–8588, Japan
[3] Department of Astronomical Science, School of Physical Sciences, The Graduate University for Advanced Studies (SOKENDAI), 2-21-1, Osawa, Mitaka, Tokyo, 181–8588, Japan
[4] Division of Geological and Planetary Sciences, 1200 E California Boulevard, Pasadena, CA 91125, USA
[5] Department of Astronomy, California Institute of Technology, Pasadena, CA 91125, USA
[6] NASA Sagan Fellow
[7] Rheinisches Institut fuer Umweltforschung an der Universitaet zu Koeln, Aachener Strasse 209, D-50931 Koeln, Germany
[8] Institute of Planetary Research, German Aerospace Center (DLR), Rutherfordstrasse 2, D-12489 Berlin, Germany
[9] Komaba Institute for Science, The University of Tokyo, 3-8-1 Komaba, Meguro, Tokyo 153–8902, Japan
[10] Instituto de Astrofísica de Canarias (IAC), E-38205 La Laguna, Tenerife, Spain
[11] Dipartimento di Fisica, Universitá di Torino, Via P. Giuria 1, I-10125, Torino, Italy
[12] Department of Earth and Planetary Science, Graduate School of Science, The University of Tokyo, 7-3-1 Hongo, Bunkyo-ku, Tokyo 113–0033, Japan
[13] Department of Astrophysical Sciences, Princeton University, 4 Ivy Lane, Princeton, NJ 08544, USA
[14] George Mason University Department of Physics & Astronomy, 4400 University Drive, MS 3F3, Fairfax, VA 22030, USA
[15] Subaru Telescope, 650 N. Aohoku Place, Hilo, HI 96720, USA
[16] Department of Earth and Planetary Sciences, Tokyo Institute of Technology, Meguro-ku, Tokyo, 152–8551, Japan
[17] Center for Planetary Systems Habitability and McDonald Observatory, The University of Texas, Austin Texas 78730, USA
[18] Thüringer Landessternwarte Tautenburg, Sternwarte 5, D-07778 Tautenburg, Germany
[19] Department of Multi-Disciplinary Sciences, Graduate School of Arts and Sciences, The University of Tokyo, 3-8-1 Komaba, Meguro, Tokyo 153–8902, Japan
[20] Stellar Astrophysics Centre, Department of Physics and Astronomy, Aarhus University, Ny Munkegade 120, DK-8000 Aarhus C, Denmark
[21] Department of Space, Earth and Environment, Astronomy and Plasma Physics, Chalmers University of Technology, SE-412 96 Gothenburg, Sweden
[22] Institute of Engineering, Tokyo University of Agriculture and Technology, 2-24-16, Nakacho, Koganei, Tokyo, 184–8588, Japan
[23] Department of Astronomy & Astrophysics, University of Chicago, Chicago, IL 60637, USA
[24] Department of Astronomy, Graduate School of Science, The University of Tokyo, 7-3-1 Hongo, Bunkyo-ku, Tokyo 113-0033, Japan
[25] Instituto de Astrofísica de Canarias (IAC), E-38205 La Laguna, Tenerife, Spain
[26] Departamento de Astrofísica, Universidad de La Laguna (ULL), E-38206 La Laguna, Tenerife, Spain
[27] Department of Space, Earth and Environment, Chalmers University of Technology, Onsala Space Observatory, SE-439 92 Onsala, Sweden
[28] Astronomy Department and Van Vleck Observatory, Wesleyan University, Middletown, CT 06459, USA
[29] Jet Propulsion Laboratory, California Institute of Technology, Pasadena, CA 91109, USA
[30] Institute of Planetary Research, German Aerospace Center, Rutherfordstrasse 2, D-12489 Berlin, Germany
[31] Mullard Space Science Laboratory, University College London, Holmbury St Mary, Dorking, Surrey RH5 6NT, UK

Abstract

We report on the discovery of an Earth-sized transiting planet ($R_p = 1.015 \pm 0.051\,R_\oplus$) in a $P = 4.02$ day orbit around K2-415 (EPIC 211414619), an M5V star at 22 pc. The planet candidate was first identified by analyzing the light-curve data obtained by the K2 mission, and it is here shown to exist in the most recent data from TESS. Combining the light curves with the data secured by our follow-up observations, including high-resolution imaging and near-infrared spectroscopy with IRD, we rule out false-positive scenarios, finding a low false-positive probability of 2×10^{-4}. Based on IRD's radial velocities of K2-415, which were sparsely taken over three years, we obtain a planet mass of $3.0 \pm 2.7\,M_\oplus$ ($M_p < 7.5\,M_\oplus$ at 95% confidence) for K2-415b. Being one of the lowest-mass stars ($\approx 0.16\,M_\odot$) known to host an Earth-sized transiting planet, K2-415 will be an interesting target for further follow-up observations, including additional radial velocity monitoring and transit spectroscopy.

Unified Astronomy Thesaurus concepts: Transit photometry (1709); High angular resolution (2167); High-resolution spectroscopy (2096); Exoplanet formation (492); Radial velocity (1332)

1. Introduction

In the era of characterizing temperate "Earth-like" planets from space (e.g., with JWST; Gardner et al. 2006) and the ground (e.g., with 30 m class telescopes), the lowest-mass stars ($\lesssim 0.3\,M_\odot$) are some of the highest-priority targets for detailed

atmospheric characterizations, such as by transmission spectroscopy, by virtue of the enhanced relative scale heights and relative closeness of the habitable zone to the host stars (which provides more opportunities to observe its transits). Obviously, the nearest examples of low-mass stars are of particular importance, given their brightness and thus the relative ease of follow-up observations. However, the number of known Earth-sized ($<1.25\,R_\oplus$) transiting planets around such nearby low-mass stars is very limited at this point: 14 planets in eight systems within 30 pc as of 2023 January,[32] including the seven around TRAPPIST-1 (Gillon et al. 2017).

The atmospheres and habitability of small rocky planets around pre-main-sequence (pre-MS; Ramirez & Kaltenegger 2014) and MS M-type dwarf stars (e.g., Kopparapu et al. 2016) are a subject of debate; low-mass stars are known to be more X-ray and extreme UV (XUV) active and exhibit a higher level of flare activity (Bogner et al. 2022), which can transform (or potentially blow off) a small planet's primordial atmosphere (e.g., Lopez & Fortney 2014) or drive the escape of water on billion-year timescales (e.g., Luger & Barnes 2015; Johnstone 2020). In addition, they spend a longer time in the pre-MS phase, implying that close-in planets around low-mass stars are more susceptible to nonthermal atmospheric erosion by high-energy protons and electrons associated with coronal mass ejections and/or stellar winds (e.g., Lammer et al. 2007). This atmospheric loss/evolution may also lead to the formation of dense secondary atmospheres on these small planets through geological processes such as volcanic eruptions, impact-induced outgassing (e.g., Elkins-Tanton & Seager 2008), and interactions between primordial atmospheres and magma oceans (e.g., Ikoma & Genda 2006; Kite & Schaefer 2021; Lichtenberg et al. 2021; Schlichting & Young 2022). Thus, small planets around M dwarfs are a good laboratory to explore the atmospheric diversity of rocky planets and the conditions at which a habitable terrestrial planet can exist.

Besides the astrobiological advantages, low-mass stars are intriguing targets as regards planet formation and evolution. Planet demographics for low-mass stars revealed interesting patterns such as the population of ultra-short-period (USP) planets (Winn et al. 2018), properties of the radius and density gaps (e.g., Van Eylen et al. 2021; Luque & Pallé 2022), and stellar-metallicity correlation with planet size (e.g., Hirano et al. 2018), most of which seem to be attributable to the different properties of protoplanetary disks and star–planet interactions around low-mass stars (e.g., Owen & Wu 2013; Dawson et al. 2015; Owen & Wu 2017; Millholland & Spalding 2020). There has been good evidence that the occurrence rate of close-in planets grows as their host stars become cooler (e.g., Dressing & Charbonneau 2015; Gaidos et al. 2016; Hardegree-Ullman et al. 2019; Sabotta et al. 2021), but the latest statistics based on the planet yields by the Transiting Exoplanet Survey Satellite (TESS; Ricker et al. 2015) suggest a lack of detected planets around the lowest-mass stars (Brady & Bean 2022), which is at least partly supported by recent population synthesis models (e.g., Burn et al. 2021). Although these findings potentially have a significant impact on planet formation theory for low-mass stars, they should be corroborated with a much larger sample size, together with an extension toward even lower masses ($\lesssim 0.2\,M_\odot$).

---

[32] https://exoplanetarchive.ipac.caltech.edu

Table 1
Stellar Parameters of K2-415 (EPIC 211414619)

Parameter	Value	Reference
(Literature Values)		
LSPM ID	J0908 + 1151	(a)
TIC ID	323687123	(b)
TOI Number	5557	(c)
α (J2000)	09:08:48.855	(d)
δ (J2000)	+11:51:41.116	(d)
$\mu_\alpha \cos\delta$ (mas yr^{-1})	-458.503 ± 0.021	(d)
μ_δ (mas yr^{-1})	192.574 ± 0.016	(d)
Parallax (mas)	45.8625 ± 0.0196	(d)
V (mag)	15.330 ± 0.027	(e)
Gaia (mag)	13.7957 ± 0.0004	(d)
TESS (mag)	12.4289 ± 0.0073	(b)
J (mag)	10.739 ± 0.026	(f)
H (mag)	10.170 ± 0.023	(f)
K (mag)	9.899 ± 0.023	(f)
Spectral type	M5V	(g)
EWHα (Å)	-1.4600 ± 0.0036	(h)
(Derived Values)		
d (pc)	21.8043 ± 0.0093	(i)
$T_{\rm eff}$ (K)	3173 ± 53	(i)
[Fe/H] (dex)	-0.13 ± 0.18	(i)
[Na/H] (dex)	-0.12 ± 0.24	(i)
[Mg/H] (dex)	-0.09 ± 0.30	(i)
[Ca/H] (dex)	-0.18 ± 0.21	(i)
[Ti/H] (dex)	0.21 ± 0.34	(i)
[Cr/H] (dex)	-0.17 ± 0.16	(i)
[Mn/H] (dex)	-0.10 ± 0.26	(i)
[Sr/H] (dex)	-0.05 ± 0.29	(i)
$\log g$ (cgs)	5.066 ± 0.027	(i)
$M_\star$ ($M_\odot$)	0.1635 ± 0.0041	(i)
$R_\star$ ($R_\odot$)	0.1965 ± 0.0058	(i)
$\rho_\star$ (g cm^{-3})	$30.3^{+2.9}_{-2.6}$	(i)
$L_\star$ ($L_\odot$)	$0.00351^{+0.00033}_{-0.00030}$	(i)
Systemic RV (km s^{-1})	22.5 ± 0.1	(i)
U (km s^{-1})	-53.72 ± 0.07	(i)
V (km s^{-1})	6.53 ± 0.05	(i)
W (km s^{-1})	-14.83 ± 0.06	(i)

Notes. References: (a) Lépine & Shara 2005; (b) Stassun et al. 2019; (c) Guerrero et al. 2021; (d) Gaia Collaboration et al. 2021; (e) Henden et al. 2016; (f) Skrutskie et al. 2006; (g) Koizumi et al. 2021; (h) https://dr7.lamost.org/, (i) this work.

In this paper, we report on the detection and follow-up observations of a new transiting planet around K2-415 (EPIC 211414619), an M5V star ≈ 22 pc from Earth (Table 1). Kepler's repurposed mission, K2 (Howell et al. 2014), first obtained light curves for the star in 2017, and our analysis using our own transit detection/vetting pipeline identified an Earth-sized planet candidate in a $P = 4.02$ days orbit, in the framework of the KESPRINT consortium: KESPRINT is an international consortium of scientists attempting to detect and characterize transiting exoplanets identified by space-based missions (e.g., Sanchis-Ojeda et al. 2015; Fridlund et al. 2017; Gandolfi et al. 2017). Recently, TESS observed the ecliptic plane, which provided a unique opportunity to revisit a number of K2 targets including K2-415, helping us validate new planet candidates and refine the ephemerides of known transiting planets. K2-415 is one of the lowest-mass stars ($\approx 0.16\,M_\odot$) observed by both K2 and TESS.

The rest of the paper is organized as follows. Section 2 presents the detection of the candidate transiting planet based on the K2 and TESS observations, which motivated us to pass the candidate on for further follow-up observations. These follow-up observations, including high-resolution imaging and spectroscopy, will be described in Section 3, and the detailed analyses of the light curves and the spectroscopic data will be given in Section 4. In Section 5, we discuss the future prospects for further follow-up observations. Section 6 summarizes our findings on the new planet.

2. Space Photometry and Detection of the Planet Candidate

2.1. K2 Photometry

K2-415 was observed by K2 in Campaign 16 from UT 2017 December 13 to UT 2018 February 25 in the long-cadence (30 minutes) mode. We reduced the target pixel files downloaded from the Mikulski Archive for Space Telescopes (MAST) website.[33] Our pipeline for reducing K2 data, searching for transiting planets, and vetting the planet candidates was detailed in Hirano et al. (2018). The major challenge in reducing K2 data was to mitigate the systematic variation due to the rolling motion of the telescope along the boresight (Howell et al. 2014). We decorrelated the flux variation with the flux centroid motion using a method similar to that described by Vanderburg & Johnson (2014). We then detrended the light curve with a cubic spline as a function of time with a width of 0.75 day to remove long-term systematics and stellar activity. We note that this spline-detrending was only used to empirically normalize the light curve for planet detection. A more physically motivated modeling of the light curve using Gaussian Process regression was also conducted as described in Section 4.4. A (BLS; Kovács et al. 2002) search returned a strong detection with a signal detection efficiency (SDE) of 12.9 at an orbital period of 4.02 day. We checked this transit signal for odd–even variation and deep secondary eclipse, which are typical signs of a false positive due to eclipsing binaries. We only detected a $2.4\,\sigma$ odd–even variation and a 0.9σ secondary eclipse (with the derived depth of 0.00014 ± 0.00015). K2-415 hence passed our initial vetting and was promoted for further follow-up observations.

2.2. TESS Photometry

K2-415 was also observed by TESS at a 2 minutes cadence with the TIC ID of 323687123 in Sectors 44, 45, and 46, between UT 2021 October 21 and December 30. In order to see if the transit signals by the same planet candidate ($P = 4.02$ days) are identifiable in the TESS data, we downloaded the PDCSAP FLUX light-curve data generated by the SPOC pipeline (Smith et al. 2012; Stumpe et al. 2012, 2014). After applying a $3.5\,\sigma$ clipping to the flux data as well as correcting for the flux offsets between different sectors (panel (b) of Figure 1), we implemented the BLS analysis (Kovács et al. 2002) as in the case of the K2 light curve. We identified the same transiting-planet candidate ($P = 4.02$ days) as the highest power in the BLS periodogram, with an SDE of 10.0 (Figure 2). This $P = 4.02$ days planet candidate was

independently detected by the TESS project, by which K2-415 was named "TOI-5557."

In order to search for an additional transiting-planet candidate in the system, we performed a joint BLS analysis using both K2 and TESS light curves. However, no significant peak other than the $P = 4.02$ day candidate was identified in the BLS periodogram.

3. Follow-up Observations

In order to confirm the planetary nature of the transiting-planet candidate identified in the K2 and TESS data, we conducted follow-up observations as below.

3.1. AO Imaging with Subaru/IRCS

On UT 2018 June 18, we performed high-resolution imaging for K2-415 using the InfraRed Camera and Spectrograph (IRCS; Kobayashi et al. 2000) and the adaptive-optics system AO188 (Hayano et al. 2008), both mounted on the Subaru 8.2 m telescope. Adopting the fine-sampling mode (1 pix = 20 mas) and the $K'-$band filter ($\approx 2.1\,\mu$m), we imaged K2-415 with a five-point dithering. The exposure time for each dithering position was set to $3\,\text{s} \times 3\,\text{coadd} = 9\,\text{s}$ so that the peak count of K2-415's image stays within the linearity count regime. We obtained two sequences of the dithering pattern, giving a total on-sky integration time of 90 s.

Raw IRCS frames were reduced as in Hirano et al. (2016), and we aligned and median-combined the reduced images in order to suppress the background noise and thus achieve a higher flux contrast. The background flux scatter in the combined image was found to be 5.9 ADU, while the flux peak of K2-415 was $\approx 11{,}400$ ADU. The full width at the half maximum (FWHM) of K2-415's image was measured to be $0.''133$, and no secondary source was detected in the field of view (FoV) of $20'' \times 20''$. To gain a constraint on the magnitude of any secondary source, we computed a $5\,\sigma$ contrast as a function of angular separation from the target, following the procedure in Hirano et al. (2016). The $5\,\sigma$ contrast curve is plotted in Figure 3, in which the inset displays the $4'' \times 4''$ image of K2-415. IRCS AO imaging achieved $\Delta m_{K'}$ of 6–7 mag at the angular separation of $1''$.

3.2. Speckle Observation with WIYN/NESSI

On the night of UT 2019 January 20, K2-415 was observed with the NESSI speckle imager (Scott 2019), mounted on the 3.5 m WIYN telescope at Kitt Peak. NESSI simultaneously acquires data in two bands centered at 562 and 832 nm using high-speed electron-multiplying CCDs (EMCCDs). We collected and reduced the data following the procedures described in Howell et al. (2011). The resulting reconstructed 832 nm band image achieved respective contrasts of Δmag ~ 4 and Δmag ~ 6 at separations of $0.''2$ and $1''$ (see Figure 4).

3.3. High-resolution Spectroscopy with Subaru/IRD

As part of the follow-up campaign for transiting-planet candidates identified by K2 and TESS, we conducted high-resolution spectroscopy using the InfraRed Doppler spectrograph (IRD; Tamura et al. 2012; Kotani et al. 2018) on the Subaru telescope. IRD covers the near-IR wavelengths from 970 to 1730 nm with a spectral resolution of $R \approx 70{,}000$. The IRD observations were carried out between UT 2019 January 15
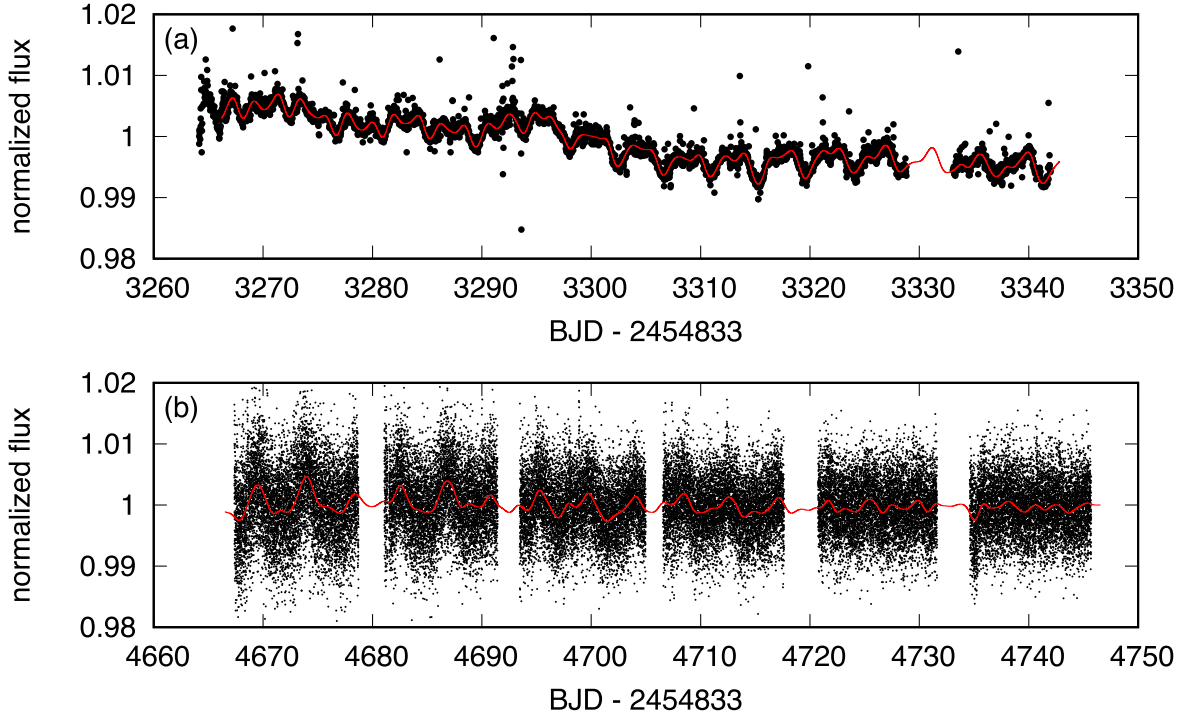

Figure 1. Light curves of K2-415 obtained by K2 (top; K2SFF) and TESS (bottom; PDC-SAP). Those data were taken at long ($\approx$29 minutes) and short (2 minutes) cadences for K2 and TESS light curves, respectively. The red solid line in each panel represents the GP regression to the observed light curve (see Section 4.4).
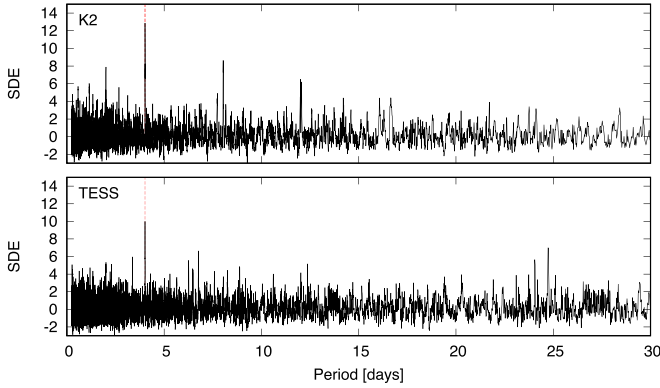

Figure 2. BLS transit signal detections for the K2 (top) and TESS (bottom) light curves. The red dashed line represents the orbital period of K2-415b (4.02 days).

Figure 3. Sensitivity plot (5σ contrast curve) for K2-415 in the K' band, based on the combined IRCS image. The inset shows a zoomed-in image of the target with an FoV of $4'' \times 4''$.

and 2022 May 25, and a total of 42 IRD frames were obtained, including a few frames taken in the Subaru Strategic Program (SSP), which is a blind Doppler survey to find exoplanets around nearby mid- to late-M dwarfs (see, e.g., Harakawa et al. 2022). For the nine frames secured in 2022 January, only H-band spectra (1450 nm $< \lambda$) were obtained, due to technical issues in the YJ-band detector. We set each integration time to 300–1800 s with a median exposure of 1200 s. For each integration, we simultaneously took the reference spectrum of the laser-frequency comb (LFC), which is used for the estimation of the instantaneous instrumental profile (IP) of the spectrograph.

Raw IRD frames were reduced as in Hirano et al. (2020), and we extracted the wavelength-calibrated one-dimensional (1D) spectra for both stellar and reference (LFC) fibers. Based on those reduced spectra, we measured precise RVs using IRD's RV-analysis pipeline (Hirano et al. 2020); briefly speaking, the instantaneous IP for each spectral segment was first estimated from the LFC spectrum, with which individual stellar spectra
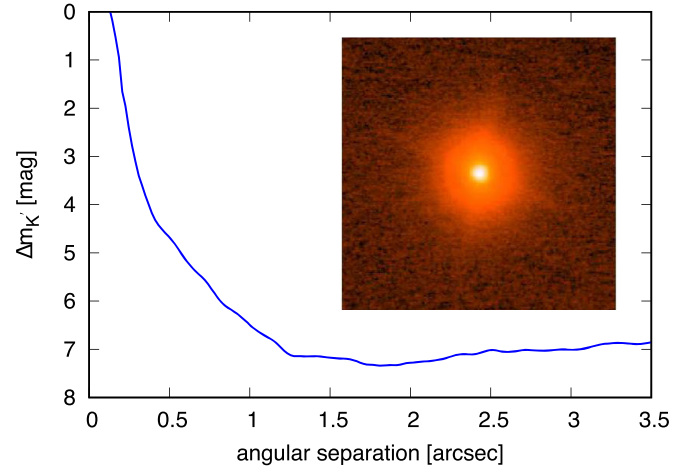
were deconvolved. The stellar template spectrum for K2-415 was then generated by combining those IP-deconvolved spectra, in which telluric lines were also removed via theoretical telluric model fits or using a rapid rotator's spectrum. The combined template was found to have good signal-to-noise (S/N) ratios (typically $>$100 per pixel) for the whole spectral range covered by IRD. Finally, relative RV ($v_\star$) with respect to this template (denoted by $S(\lambda)$) was measured by forward-modeling each observed spectral segment ($f_{\rm obs}(\lambda)$) as

$$f_{\rm obs}(\lambda) = k(\lambda)\left[S\left(\lambda \sqrt{\frac{1 + v_\star/c}{1 - v_\star/c}} \right) T(\lambda) \right] * {\rm IP}, \qquad (1)$$
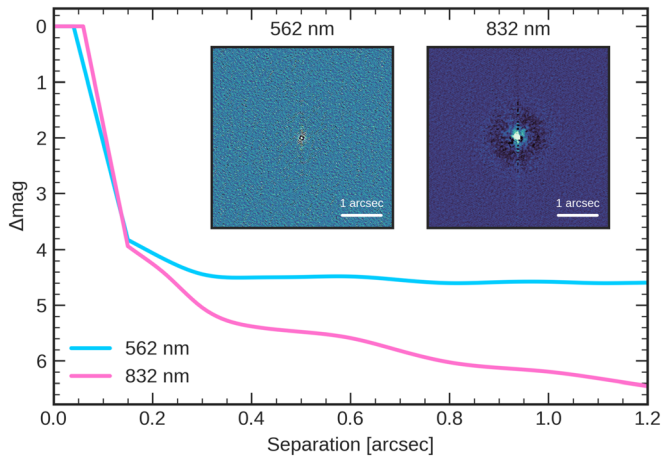
Figure 4. Sensitivity plots of K2-415, based on the speckle observations by NESSI. The two insets display the reconstructed images of K2-415 in the 562 nm (left) and 832 nm (right) bands.

where $T(\lambda)$ is the theoretical telluric model and $k(\lambda)$ is a second-order polynomial describing the spectrum continuum for each segment (see Hirano et al. 2020, for more details). The resulting relative RVs are listed in Table 2. The typical RV uncertainty (internal error) was 4–7 m s^{-1}. We also estimated the absolute RV of K2-415 by fitting the individual molecular lines in the IRD spectra via Gaussian functions and comparing their centers with the vacuum line positions in the literature. Based on the analysis of 37 relatively deep OH lines in the H band, we obtained a mean absolute RV of 22.5 ± 0.1 km s^{-1}.

4. Analyses and Results

4.1. Estimation of Stellar Parameters

Using K2-415's template spectrum produced in Section 3.3, we performed a line-by-line analysis to estimate the stellar atmospheric parameters. We measured equivalent widths of FeH molecular lines and atomic lines of Na, Mg, Ca, Ti, Cr, Mn, Fe, and Sr to derive an effective temperature T_{eff} and abundances of individual elements [X/H]. For the T_{eff} estimation, 47 well-isolated FeH lines in the Wing–Ford band at 990–1020 nm were employed in the procedure described by Ishikawa et al. (2022). For the abundance analysis, we analyzed 33 atomic lines by following the procedure of Ishikawa et al. (2020).

We iterated the T_{eff} estimation and the abundance analysis alternately until both results became consistent with each other. First, we derived a provisional T_{eff} by adopting the solar metallicity as the initial value, and then by adopting this provisional T_{eff}, we derived the individual abundances of the eight elements. Subsequently, we adopted the iron abundance [Fe/H] derived in the previous step as the input metallicity of the T_{eff} estimation. Finally, adopting the new T_{eff} value, we redetermined the elemental abundances. The procedure up to this point allows the inputs and outputs of the analyses to be consistent within the measurement errors.

The final results of the T_{eff} and the elemental abundances are listed in Table 1. Note that the uncertainty of the T_{eff} here is calculated by the standard deviation of the estimates from the individual FeH lines, while it may also have a systematic error of less than 100 K as discussed in Ishikawa et al. (2022).

Based on those atmospheric parameters, we also derived the other physical parameters of K2-415. Inputting the above-derived metallicity [Fe/H] as well as 2MASS's K_s-band magnitude (Skrutskie et al. 2006) and Gaia parallax (Gaia Collaboration et al. 2021), we derived the stellar mass $M_\star$ and radius $R_\star$ using the empirical relations by Mann et al. (2019) and Mann et al. (2015), respectively. The uncertainties of those parameters were calculated with Monte Carlo simulations, assuming Gaussian distributions for the above input parameters and systematic errors in the empirical formula (Mann et al. 2019). In the Monte Carlo calculations, we derived the surface gravity log g, mean stellar density $\rho_\star$, and luminosity $L_\star$. We also computed the Galactic (U, V, and W) velocities with respect to the Sun, using the Gaia DR3 information as well as the systemic RV (Table 1). All of those derived parameters are also summarized in Table 1. The low kinematic velocities indicate that K2-415 is a thin disk star.

Both K2 and TESS light curves in Figure 1 exhibit flux variations that are representative of spot-induced rotational modulations. To estimate the rotation period of K2-415, we computed the generalized Lomb–Scargle (LS) periodogram (Zechmeister & Kürster 2009) for the two light curves. As shown in Figure 5, both periodograms show strong peaks at similar periods, whose powers correspond to false-alarm probabilities (FAP) much lower than 10^{-3}. Inspecting the peaks of the periodograms as well as the shapes of original light curves, we estimated the rotation period of the star to be $P_{rot} = 4.36 \pm 0.15$ days for K2 and $P_{rot} = 4.26 \pm 0.12$ days for TESS light curves, respectively. The uncertainties of these periods were derived based on the FWHMs of the peaks.

The clear photometric variability (with the amplitude of 0.2%–0.4%) as well as the relatively short period of rotation suggests that K2-415 is a moderately active star. Inspecting an archived optical spectrum of K2-415 observed by the Large Sky Area Multi-Object Fiber Spectroscopic Telescope (LAMOST; Luo et al. 2015), we checked for its chromospheric activity. As shown in Figure 6, K2-415's low-resolution spectrum exhibits a moderate emission at Hα, whose EW is measured to be EWH$\alpha = -1.4600 \pm 0.0036$ Å[34] (a negative value of EW indicates that it is an emission line), in agreement with the moderate variability seen in the light curves. We note that the variability amplitude of light-curve modulations seems to evolve rapidly in time, as evidenced by the vanishing variation in the second half of the TESS data. This fact suggests that activity-induced spectroscopic variations such as RV jitters do not produce a coherent pattern even on a timescale of 1–2 months. We will discuss the spot-induced photometric and spectroscopic variabilities in more detail in Section 4.4.

4.2. Joint Analyses of Transit Photometry

Because two different sets of light curves (K2 and TESS) are available for K2-415, we first analyzed each data set independently, to check for consistency in the derived parameters (e.g., transit depth). For the transit analysis of K2 data, we ended up using the public light curve, K2SFF (Vanderburg & Johnson 2014), as K2SFF generally delivers better-quality light curves than our own ones (Section 2.1) in terms of flux scatters and behavior of outliers. Following the procedure in Hirano et al. (2015), we extracted light-curve segments around the transits (assuming a constant period, with

---

[34] https://dr7.lamost.org

5

Table 2
RVs and Spectral Indices Extracted from IRD Spectra

| Time (BJD$_{TDB}$)	Relative RV (m s^{-1})	RV Error (m s^{-1})	ΔFWHM (km s^{-1})	ΔFWHM Error (km s^{-1})	ΔBIS (km s^{-1})	ΔBIS Error (km s^{-1})
2458498.9140269	6.1	4.7	−0.024	0.038	0.19	0.18
2458498.9293007	−6.5	5.5	−0.170	0.044	−0.10	0.11
2458499.8875579	−15.1	4.6	−0.115	0.036	0.14	0.18
2458499.9053351	−3.5	4.4	−0.126	0.034	0.20	0.13
2458499.9231437	3.1	4.4	−0.087	0.033	0.23	0.14
2458563.8273755	0.8	3.7	−0.066	0.036	0.06	0.15
2458563.8434206	−0.2	4.1	−0.005	0.041	0.18	0.14
2458563.8576999	−2.6	4.3	−0.113	0.040	0.02	0.13
2458626.8089605	−3.5	10.9	−0.151	0.102	−0.02	0.21
2458626.8127899	−33.4	10.2	−0.351	0.091	0.10	0.20
2458626.8164678	0.8	10.2	−0.149	0.095	0.15	0.24
2458649.7618439	3.1	6.5	−0.229	0.063	−0.03	0.13
2458649.7691465	−3.3	7.1	−0.068	0.069	0.09	0.18
2458649.7764790	7.5	7.1	−0.078	0.071	−0.07	0.13
2458828.0584522	−0.7	4.9	−0.100	0.047	0.02	0.14
2458896.0058500	10.7	10.0	−0.109	0.092	0.43	0.26
2458896.0167066	0.2	7.2	0.043	0.068	0.53	0.26
2459244.9776946	−3.7	4.8	0.014	0.045	0.14	0.21
2459247.9043374	−3.2	4.9	0.051	0.045	−0.32	0.25
2459275.9973405	−6.2	6.1	−0.020	0.057	−0.08	0.13
2459276.0151846	16.0	9.8	−0.205	0.089	−0.07	0.20
2459321.8971738	27.1	5.8	−0.124	0.055	0.06	0.47
2459321.9113889	4.8	5.4	0.029	0.050	−0.15	0.15
2459323.7582073	12.9	4.5	0.143	0.041	0.10	0.17
2459323.7724223	16.3	4.5	0.021	0.042	−0.09	0.15
2459328.7606870	29.7	5.5	−0.020	0.050	−0.03	0.13
2459328.7749031	12.0	5.3	−0.069	0.052	0.13	0.21
2459337.7794598	4.0	9.6	0.040	0.091	0.14	0.23
2459338.7871978	2.6	5.0	−0.044	0.040	0.03	0.11
2459588.1189335	12.8	6.4	0.055	0.042	0.41	0.17
2459589.1004307	14.3	6.1	−0.036	0.038	0.19	0.18
2459589.1182238	17.9	6.1	−0.163	0.036	0.22	0.13
2459596.8815868	2.0	6.4	−0.026	0.049	0.39	0.23
2459596.8996175	−9.9	6.4	−0.008	0.049	0.55	0.21
2459602.1065831	−2.3	11.3	0.478	0.097	−0.24	0.35
2459602.1209018	4.1	12.3	0.347	0.104	−0.04	0.32
2459604.0756268	−8.3	5.2	0.072	0.040	−0.01	0.21
2459604.0969686	−20.9	5.2	0.029	0.040	0.01	0.22
2459648.9839188	−10.0	8.9	−0.013	0.081	0.28	0.18
2459711.7427174	−14.1	6.3	−0.035	0.058	0.32	0.16
2459711.7569324	−12.9	6.3	0.010	0.060	0.22	0.18
2459724.7450558	−2.9	4.8	−0.045	0.046	0.22	0.12
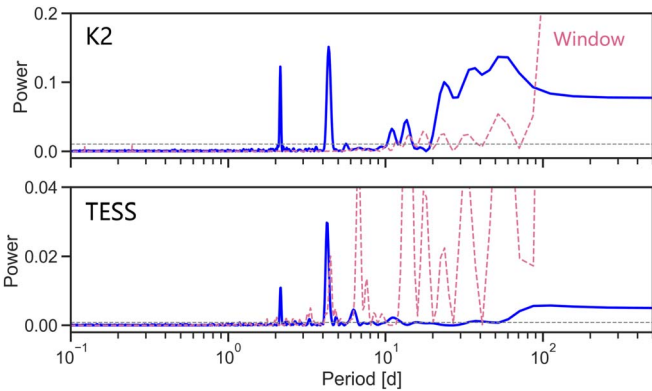
Figure 5. LS periodograms for the K2 (top) and TESS (bottom) light curves. The window function for each light curve is plotted by the dashed line. The secondary peak at ≈2 days represents the harmonics of the rotation period.

a period based on a preliminary fit), and simultaneously fitted all the extracted segments while allowing for possible transit timing variations (TTVs). Each extracted segment covers approximately 5× the transit duration, thus typically involving 8–10 flux points. We implemented a Markov Chain Monte Carlo (MCMC) analysis to fit the light-curve segments after a global optimization of the fitting parameters using Powell's conjugate direction method as in Hirano et al. (2015). In the analysis, we employed the transit model by Ohta et al. (2009) and a linear function of time for the out-of-transit baseline. To take into account the ≈29 minute cadence of K2 photometry, for each observed flux we computed the transit model with one-minute sampling and binned the light curve to the K2 sampling. The fitting parameters are the scaled semimajor axis $a/R_\star$, transit impact parameter b, star-to-planet radius ratio $R_p/R_\star$, limb-darkening parameters in the quadratic law (u_1 and u_2),
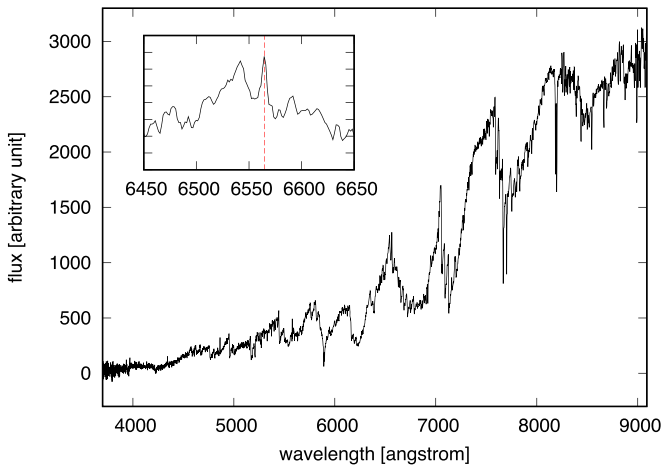
Figure 6. Low-resolution optical spectrum of K2-415 obtained by LAMOST (Luo et al. 2015). The inset displays a zoom-in around Hα (the red vertical line).

orbital period P, and mid-transit time for each transit $T_c^{(i)}$. We fixed the orbital eccentricity at $e = 0$ at this point. Only for the limb-darkening parameters, we imposed Gaussian priors as $u_1 + u_2 = 0.81 \pm 0.20$ and $u_1 - u_2 = 0.00 \pm 0.20$, based on the theoretical calculations by Claret et al. (2013). The result of this MCMC analysis is given in the leftmost column of Table 3. From the mid-transit times for individual transits, we also computed the zero-point mid-transit time $T_{c,0}$ for the K2 data set, assuming a linear ephemeris (i.e., a constant period).

We also analyzed the TESS light curve (PDCSAP FLUX), following the same procedure as above. The only differences in the modeling are that we did not integrate the theoretical transit model for TESS data (2 minutes cadence) and we adopted different priors for the limb-darkening parameters ($u_1 + u_2 = 0.73 \pm 0.20$ and $u_1 - u_2 = -0.17 \pm 0.20$ for the TESS band). The result of the MCMC fit to the TESS light curve is presented in the second column of Table 3.

The transit parameters ($R_p/R_\star$ and P in particular) derived from K2 and TESS light curves are consistent with one another within 1σ, suggesting that no significant dilution is blended in those light curves, given that they were obtained with different apertures and different pass bands. The respective stellar densities estimated from the transit modeling are 47^{+51}_{-39} g cm^{-3} for K2 and 24^{+13}_{-17} g cm^{-3} for TESS light curves. Although these are both compatible with the mean stellar density derived in Section 4.1 ($\rho_\star = 30.3^{+2.9}_{-2.6}$ g cm^{-3}), the constraint is rather weak due to the degeneracy in $a/R_\star$, b, and $R_p/R_\star$ in the transit modeling. Figure 7 plots the observed minus calculated $(O - C)$ residuals from the linear ephemeris for the transit times derived from the K2 (top) and TESS (bottom) data sets. No significant TTVs are seen for either data set; the χ^2 statistics for the transit times are 15.2 (K2) and 16.3 (TESS), with the degrees of freedom being 15 and 16, respectively. We also ensured that the two $T_{c,0}$ values derived from the K2 and TESS data sets are compatible with each other once P's error propagation is taken into account.

Satisfied with the results of these consistency checks, we next performed joint analyses of K2 and TESS light curves. Based on the lack of TTVs, in the joint analyses we did not allow for a variable T_c for each transit, but instead allowed only the period P and global zero-point $T_{c,0}$ to float freely. In addition, to help break the degeneracy between $a/R_\star$ and b, we

imposed a Gaussian prior on the stellar density as $\rho_\star = 30.5 \pm 2.7$ g cm^{-1}, based on Table 1 in the MCMC analysis. We jointly modeled and fitted all the light-curve segments from the K2 and TESS data, and we derived the global posterior distribution for the fitting parameters.

In this joint analysis, we tried two different fits: one with $e = 0$ and the other with a floating e. The result of the $e = 0$ model fit is presented in the third column of Table 3. The derived parameters are in good agreement with the ones derived from fitting the K2 or TESS light curve alone, but with much smaller uncertainties. For the floating e model, we first attempted an MCMC analysis allowing $\sqrt{e} \cos\omega$ and $\sqrt{e} \sin\omega$ to vary freely, but we found the fit did not converge, likely owing to the degeneracy in the fitting parameters together with the shallow transit and very short transit duration (see, e.g., Serrano et al. 2022). Orbital eccentricities of close-in planets have been studied in the past, and low or moderate eccentricities were suggested for small, close-in planets (e.g., Mayor et al. 2011; Van Eylen et al. 2019). Thus, we imposed weak Gaussian priors on $\sqrt{e} \cos\omega$ and $\sqrt{e} \sin\omega$, with a mean and standard deviation of 0 and 0.335, respectively, so that the 1σ upper limit of e becomes 0.45 (Mayor et al. 2011). These priors were used only to account for the uncertainty in e and derive realistic errors for the other fitting parameters. The result of this MCMC fit for the $e \neq 0$ model is shown in the rightmost column of Table 3. The phase-folded transit light curves after corrections for the out-of-transit baseline are plotted in Figure 8, along with the best-fit transit models.

4.3. Statistical Validation of K2-415b

We computed the false-positive probability (FPP) of K2-415b using the Python package vespa (Morton 2015), which was developed for the statistical validation of planets from the Kepler mission (Morton et al. 2016). vespa employs a robust statistical framework to compare the likelihood of the planetary scenario to the likelihoods of several astrophysical false-positive scenarios involving eclipsing binaries, relying on simulated eclipsing populations based on the TRILEGAL galaxy model (Girardi et al. 2005). As inputs to vespa, we used an exclusion radius of 4″, WIYN/NESSI contrast curves (Section 3.2), phase-folded TESS photometry, and a 3σ upper limit on the secondary eclipse depth (Section 2.1), as well as broadband optical and NIR photometry, the Gaia parallax, and our spectroscopically derived estimates of the effective temperature and metallicity of the host star (Table 1). The FPP from vespa for K2-415b is 2×10^{-4}, well below the commonly used validation threshold of 1%, which is in good agreement with the nondetection of any massive companions in our high-resolution imaging and RV measurements.

To confirm the low FPP, we also implemented another Python package, TRICERATOPS (Giacalone et al. 2021), which was developed to vet and validate TESS planet candidates. TRICERATOPS also returned a low FPP of 0.15% for K2-415b, confirming the result by vespa. K2-415b is therefore incompatible with any known false-positive scenarios, so we conclude that it has to be a real planet.

4.4. Analyses of IRD Data

RV data presented in Table 2 show a relatively large scatter with a root-mean-square (rms) of 11.9 m s^{-1}, which is significantly larger than the mean RV internal error of 6.5 m s^{-1}. The expected

Table 3
Results of Transit Analyses for K2-415b

Data Set	K2 ($e = 0$)	TESS ($e = 0$)	K2 + TESS ($e = 0$)	K2 + TESS (e prior)
(Fitting Parameter)				
$a/R_\star$	34^{+10}_{-16}	$27.4^{+4.2}_{-9.3}$	$29.74^{+0.83}_{-0.91}$	$29.63^{+0.86}_{-0.91}$
b	$0.52^{+0.39}_{-0.36}$	$0.43^{+0.37}_{-0.30}$	$0.39^{+0.11}_{-0.18}$	$0.37^{+0.19}_{-0.23}$
$R_p/R_\star$	$0.0513^{+0.0138}_{-0.0045}$	$0.0514^{+0.0053}_{-0.0033}$	0.0470 ± 0.0018	$0.0472^{+0.0020}_{-0.0018}$
$u_1^{(K2)} + u_2^{(K2)}$	0.81 ± 0.20	...	0.79 ± 0.18	0.79 ± 0.19
$u_1^{(K2)} - u_2^{(K2)}$	-0.01 ± 0.20	...	0.00 ± 0.20	-0.01 ± 0.20
$u_1^{(TESS)} + u_2^{(TESS)}$	...	0.72 ± 0.20	0.74 ± 0.20	0.72 ± 0.19
$u_1^{(TESS)} - u_2^{(TESS)}$	...	-0.17 ± 0.20	-0.16 ± 0.20	-0.17 ± 0.20
$\sqrt{e} \cos \omega$	0 (fixed)	0 (fixed)	0 (fixed)	$0.00^{+0.29}_{-0.30}$
$\sqrt{e} \sin \omega$	0 (fixed)	0 (fixed)	0 (fixed)	$0.00^{+0.20}_{-0.25}$
P (days)	4.01780 ± 0.00019	4.01803 ± 0.00024	4.0179682 ± 0.0000021	4.0179694 ± 0.0000027
$T_{c,0} - 2454833$ (BJD)	3267.0727 ± 0.0018	4665.3230 ± 0.0033	3267.07137 ± 0.00054	3267.07116 ± 0.00069
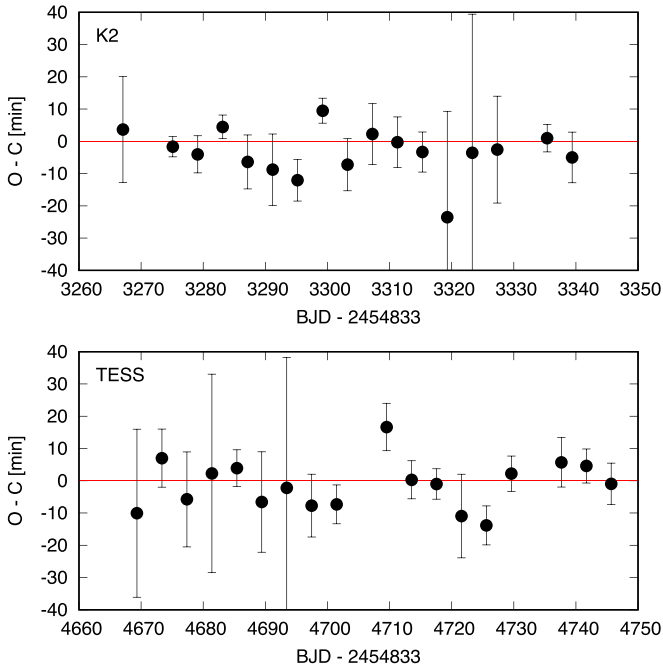
Figure 7. Residuals from the linear ephemeris (a constant period) for K2-415b's transit times for the K2 (top) and TESS (bottom) data.

RV variation by K2-415b is only a few m s^{-1}, based on the mass–radius relation (e.g., Otegi et al. 2020). In order to see if we can detect any planet signal associated with the period of K2-415b, we computed the generalized LS periodogram (Zechmeister & Kürster 2009) for the observed RV data. However, no significant peak showed up at $P = 4.02$ days, as drawn in Figure 9 (more generally, no peak exceeded the FAP = 1% threshold). While a fraction of the excess RV scatter might be ascribed to the instrumental systematics of IRD (e.g., Hirano et al. 2021; Harakawa et al. 2022), one should notice that K2-415 has a relatively short period of rotation ($P_{rot} = 4.1$–4.5 days, according to the LS periodograms) and both K2 and TESS light curves exhibit significant variations due to star spots. The stellar rotation period and the radius translate to the equatorial rotation velocity of ≈ 2.3 km s^{-1}, which places an upper limit on the $v \sin i$ of K2-415. Assuming that the system has a spin–orbit alignment (i.e., $v \sin i \approx 2.3$ km s^{-1}) and that the star has an effective surface-spot area of $\approx 0.2\%$–0.4% (from the light curves in Figure 1), one can roughly estimate the expected RV jitter amplitude as

8–16 m s^{-1} (e.g., Desort et al. 2007; Boisse et al. 2012), which is comparable to the amplitude of the excess RV scatter. Therefore, in the following discussion, we model the observed RVs while taking into account the spot-induced RV jitters, to obtain an accurate constraint on the mass of K2-415b.

To model the observed RVs, we employed the Gaussian Process (GP) based approach described in Rajpaul et al. (2015); in short, they applied the GP regression to the observed RVs together with the auxiliary parameters (the $\log R'_{HK}$ index and the inverse slope of the cross-correlation bisector (BIS)) measured from the same spectra. To implement a similar GP regression, we measured some activity indices from the IRD spectra in a manner similar to that of Harakawa et al. (2022). Because the Ca HK line is not covered by IRD, instead of $\log R'_{HK}$, we adopted the FWHM of the mean line profile, which is known to display a behavior similar to that of $\log R'_{HK}$ (Rajpaul et al. 2015). The mean line profile for each IRD spectrum is extracted using the least-squares deconvolution method (LSD; Donati et al. 1997; Asensio Ramos & Petit 2015), and in doing so, we used only OH lines, which are the most dominant opacity sources in the H-band spectra of early- to mid-M dwarfs.[35] From the same LSD profile, we also measured the BIS. For both FWHM and BIS measurements, we subtracted the temporal mean values for individual lines and averaged over many different lines in the same spectrum in order to focus on the relative variations in FWHM and BIS, which we call ΔFWHM(t) and ΔBIS(t). More details of activity-index measurements for IRD spectra will be presented in our upcoming papers. The time series and LS periodograms of ΔFWHM(t) and ΔBIS(t) are also presented in Table 2 and Figure 9, respectively.

Following Rajpaul et al. (2015), we model the stochastic component of the observed RVs (ΔRV(t)) as well as ΔFWHM(t) and ΔBIS(t) by the following equations:

$$\Delta RV(t) = V_c G(t) + V_r \dot{G}(t), \qquad (2)$$

$$\Delta FWHM(t) = W G(t), \qquad (3)$$

$$\Delta BIS(t) = B_c G(t) + B_r \dot{G}(t), \qquad (4)$$

where $G(t)$ is a latent function associated with the fractional spot area and its derivative. The coefficients V_c, V_r, W, B_c, and B_r are determined by fitting the observed data. In a

---

[35] We did not use YJ-band spectra for activity-index measurements, because a significant fraction of IRD data were taken with the H-band detector alone (see Section 3.3).
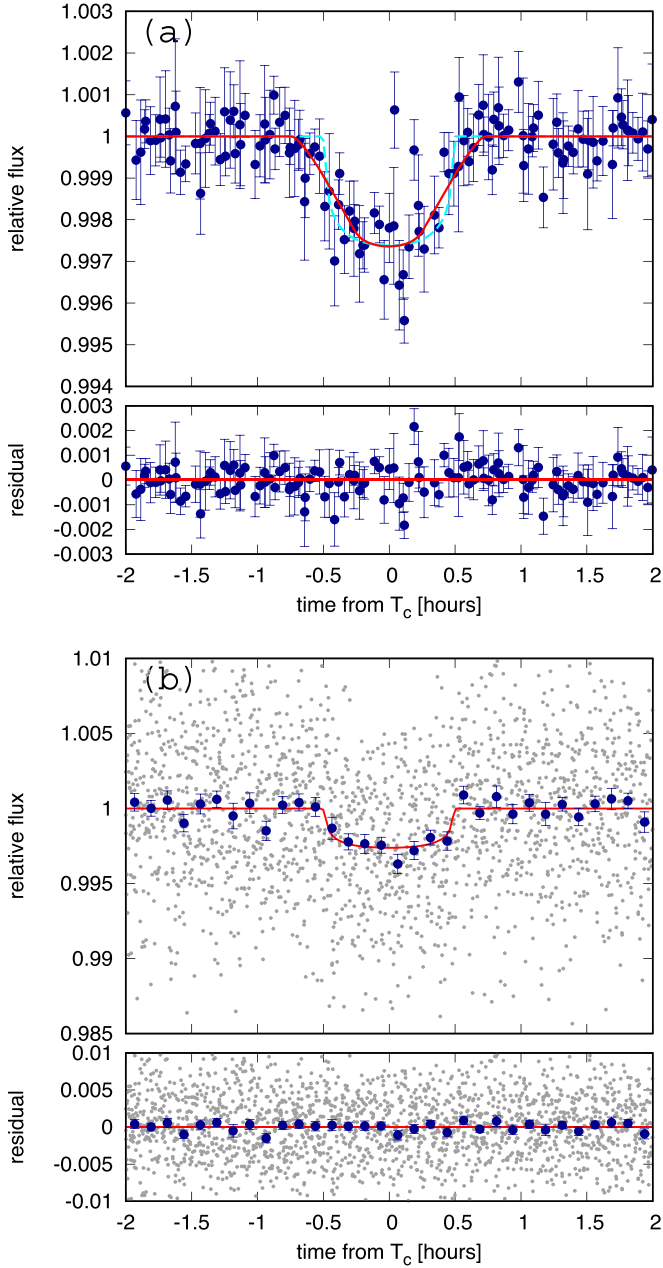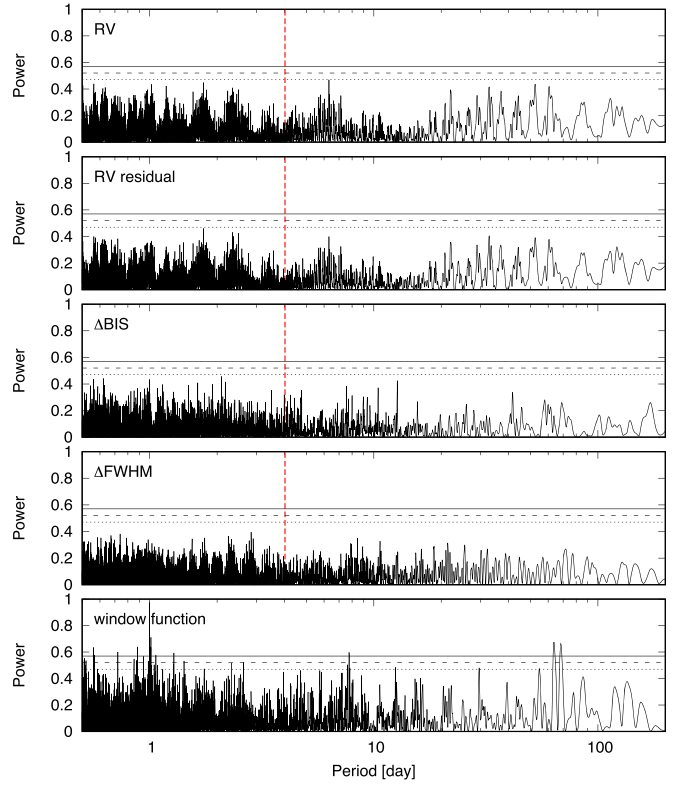
Figure 9. LS periodograms for the observed RVs and spectral indices (ΔFWHM and ΔBIS) extracted from the IRD spectra. In each panel, the vertical dashed line represents the orbital period of K2-415b. The three horizontal lines correspond to the FAPs of 5%, 1%, and 0.1% from the bottom, respectively. The second panel from the top shows the LS power for the RV residuals after subtracting the best-fit orbit of K2-415b.

variables. In our formulation, $n = 3N_{\mathrm{data}}$, with N_{data} being the number of IRD spectra ($= 42$ in the present case). We adopt the mean functions $\boldsymbol{m}$ given by

$$m_{\mathrm{RV}}(t) = K\left\{\cos(f + \omega) + e\cos\omega\right\} + \gamma_{\mathrm{RV}}, \qquad (6)$$

$$m_{\Delta\mathrm{FWHM}}(t) = \gamma_{\Delta\mathrm{FWHM}}, \qquad (7)$$

$$m_{\Delta\mathrm{BIS}}(t) = \gamma_{\Delta\mathrm{BIS}}, \qquad (8)$$

where f is the true anomaly and K is the RV semi-amplitude due to K2-415b's Keplerian motion. The constant offset γ in each variable is also optimized in the fit. For the RV modeling, a fixed orbital period P is used, based on the transit light-curve analyses in Section 4.2.

The only remaining quantity to be determined a priori is the form of the covariant matrix Σ. Here, we adopt the quasi-periodic kernel for the covariance between the latent functions $G(t_i)$ and $G(t_j)$:

$$k_{\mathrm{qp}}(t_i, t_j) \equiv \exp\left[-\frac{\sin^2\{\pi(t_i - t_j)/P_{\mathrm{rot}}'\}}{2\lambda_{\mathrm{p}}^2} - \frac{(t_i - t_j)^2}{2\lambda_{\mathrm{e}}^2}\right], \qquad (9)$$

and compute the covariant matrix Σ following the expressions given by Rajpaul et al. (2015). The hyperparameters P_{rot}', λ_{p}, and λ_{e} are also fitting parameters in the regression.

We attempted to implement a multidimensional GP regression to the observed quantities (RV, ΔFWHM(t), and ΔBIS(t)) using our custom MCMC code (Hirano et al. 2016), in which all the fitting parameters are allowed to float freely, but we

Figure 8. Folded K2 (panel (a)) and TESS (panel (b)) transit light curves of K2-415b, for which a linear ephemeris is assumed. In both panels, red solid lines indicate the best-fit transit model (the e-prior fit) for the observed data, and flux residuals from the model are plotted at the bottom. For panel (a), K2's long cadence is taken into account in drawing the best-fit theoretical curve, and the original transit model before binning is shown by the cyan dashed line in the same panel.

multidimensional GP regression, fitting parameters are optimized so that the logarithm of the likelihood function $\mathcal{L}$ is maximized:

$$\log \mathcal{L} = -\frac{1}{2}(\boldsymbol{y} - \boldsymbol{m})^{\mathrm{T}}\Sigma^{-1}(\boldsymbol{y} - \boldsymbol{m})$$
$$- \frac{1}{2}\log(|\Sigma|) - \frac{n}{2}\log(2\pi), \qquad (5)$$

where $\boldsymbol{y}$ and $\boldsymbol{m}$ are the vectors (with n components) representing the observed variables and mean functions, respectively, and Σ is the covariant matrix of the input

Table 4
GP Regressions to the Light Curves

Data Set	K2	TESS
(Fitting Parameter)		
A	$0.00288^{+0.00039}_{-0.00031}$	$0.00132^{+0.00017}_{-0.00013}$
$P'_{\rm rot}$ (days)	$4.164^{+0.084}_{-0.065}$	$4.54^{+0.10}_{-0.11}$
$\lambda_{\rm p}$	$0.692^{+0.069}_{-0.058}$	$0.411^{+0.069}_{-0.055}$
$\lambda_{\rm e}$ (days)	4.71 ± 0.23	$3.65^{+0.41}_{-0.39}$

immediately found that the fit did not converge, often resulting in walkers being stuck to different local minima. This is likely attributable to the small number of data points (only 42), spread over many years. In particular, the sparseness of the data seemed to prohibit reliable estimations of the periodicity ($P'_{\rm rot}$) and evolution timescale ($\lambda_{\rm e}$) of RV jitters. We thus resorted to a two-step approach employed by Grunblatt et al. (2015), who used the light curves to constrain the hyperparameters in the covariance kernel (Equation (9)), and performed GP regressions to the K2 and TESS data before analyzing the spectral data. Adopting the covariance matrix for the flux values, whose elements are given by

$$\Sigma_{ij} = A^2 k_{\rm qp}(t_i, t_j) + \sigma_i^2 \delta(t_i - t_j), \qquad (10)$$

where σ_i is the ith flux error, we ran MCMC analyses to estimate $P'_{\rm rot}$, $\lambda_{\rm p}$, and $\lambda_{\rm e}$ as well as the correlation amplitude A for each of K2 and TESS light curves (binned after masking the transits). The results of these analyses are presented in Table 4, and GP regressions to the light curves are plotted by the red solid lines in Figure 1. The derived parameters show a moderate disagreement ($\approx 3\sigma$ except A) between K2 and TESS data, but these are likely due to different properties of the two data sets (e.g., different observing bands) as well as data processing. The GP-based period ($P'_{\rm rot} \approx 4.2$–4.5 days) roughly agrees with the rotation period derived from the LS periodograms ($P_{\rm rot} \approx 4.3$–4.4 days; see Section 4.1), which justifies the use of the quasi-periodic kernel for the GP regression.

We computed the weighted mean for each hyperparameter in Table 4, and used the results from the light-curve analysis as priors in GP regressions for the spectral data; employing Gaussian priors of $P'_{\rm rot} = 4.291 \pm 0.061$ days, $\lambda_{\rm p} = 0.554 \pm 0.044$, and $\lambda_{\rm e} = 4.45 \pm 0.20$ days, we implemented the MCMC fit to the observed RVs along with ΔFWHM and ΔBIS. In the analysis, we introduced additional fitting parameters $C_{\rm RV}$, $C_{\Delta \rm FWHM}$, and $C_{\Delta \rm BIS}$, to take into account underestimation/overestimation for internal errors of input variables, which are inserted into the diagonal components of the covariance matrix Σ as

$$C_l^2 \sigma_i^{(l)2} \delta(t_i - t_j), \qquad (11)$$

where $l = \{$RV, $\Delta FWHM$, $\Delta BIS\}$ and $\sigma_i^{(l)}$ is the input statistical error at time t_i. We employed this formulation to model the white noise components in the fit, as opposed to adding extra terms of white noise in quadrature, because we found the input statistical errors of BIS we measured from the spectral analysis are slightly overestimated (i.e., $C_{\Delta \rm BIS} < 1.0$).

As in the case of transit photometry analyses, we tried two different fits with $e = 0$ and with priors on e. A fit with completely free $\sqrt{e} \cos \omega$ and $\sqrt{e} \sin \omega$ did not result in a meaningful constraint on e, likely due to the small number of

Table 5
GP Regressions to the IRD Data (RV + Spectral Indices)

Condition	$e = 0$	e prior
(Fitting Parameter)		
K (m s^{-1})	$4.4^{+3.1}_{-3.3}$	$4.1^{+3.5}_{-3.6}$
$\sqrt{e} \cos \omega$ *	0 (fixed)	0.03 ± 0.29
$\sqrt{e} \sin \omega$ *	0 (fixed)	0.00 ± 0.32
$\gamma_{\rm RV}$ (m s^{-1})	1.6 ± 2.4	$1.6^{+2.4}_{-2.5}$
$\gamma_{\Delta \rm FWHM}$ (km s^{-1})	-0.038 ± 0.018	-0.038 ± 0.018
$\gamma_{\Delta \rm BIS}$ (km s^{-1})	$0.098^{+0.043}_{-0.042}$	0.096 ± 0.042
$P'_{\rm rot}$ * (days)	$4.295^{+0.061}_{-0.060}$	4.298 ± 0.061
$\lambda_{\rm p}$ *	0.564 ± 0.044	0.562 ± 0.044
$\lambda_{\rm e}$ * (days)	4.46 ± 0.20	4.46 ± 0.20
V_c (m s^{-1})	$5.0^{+3.4}_{-3.3}$	5.2 ± 3.4
V_r (m s^{-1})	$-2.3^{+4.2}_{-3.5}$	$-2.5^{+4.5}_{-3.5}$
W (km s^{-1})	$0.008^{+0.041}_{-0.049}$	$0.008^{+0.039}_{-0.048}$
B_c (km s^{-1})	$0.00^{+0.12}_{-0.13}$	$-0.01^{+0.12}_{-0.13}$
B_r (km s^{-1})	$0.104^{+0.042}_{-0.052}$	$0.102^{+0.043}_{-0.053}$
$C_{\rm RV}$	$1.56^{+0.31}_{-0.24}$	$1.55^{+0.30}_{-0.24}$
$C_{\Delta \rm FWHM}$	$1.93^{+0.27}_{-0.25}$	$1.94^{+0.27}_{-0.25}$
$C_{\Delta \rm BIS}$	$0.61^{+0.15}_{-0.10}$	$0.61^{+0.15}_{-0.10}$

Note. Gaussian priors are imposed on the fitting parameters with asterisks.

data points and significant RV jitters, and hence we imposed Gaussian priors on these parameters, as in Section 4.2, only to obtain realistic uncertainties for the other fitting parameters. With all the fitting parameters other than $P'_{\rm rot}$, $\lambda_{\rm p}$, $\lambda_{\rm e}$, $\sqrt{e} \cos \omega$, and $\sqrt{e} \sin \omega$ being allowed to vary freely, we performed GP regressions to the spectral data by implementing MCMC analyses (Hirano et al. 2016). The results of these analyses are summarized in Table 5.

Figure 10 plots the time series of the observed RVs along with the two spectral indices, and the red solid line for each panel indicates the best-fit GP regression (with the e prior) to the observed data. The phase-folded RV curve after removing the GP stochastic components is given in Figure 11. The derived RV semi-amplitude K of $4.1^{+3.5}_{-3.6}$ m s^{-1} well agrees with that expected from the mass–radius relation ($K = 1$–2 m s^{-1}; Otegi et al. 2020), but it is also compatible with a nondetection of the planet within 1.1 σ, which is consistent with the lack of a significant peak at the orbital period in the LS periodogram of the RV data. Nonetheless, the 1 σ upper limit of K translates to the planet mass constraint of $<5.7 M_\oplus$, which, along with the lack of a long-term RV trend, allows us to completely rule out FP with a stellar companion.

5. Discussion

Adopting the parameters derived in Section 4 (for the e prior fit), we calculated the final planetary parameters of K2-415b, including the physical planet radius R_p, mass M_p, semimajor axis a, orbital inclination i_o, stellar insolation onto the planet S_p, and equilibrium temperature $T_{\rm eq}$, for which we adopted two Bond albedos: $A_B = 0$ and $A_B = 0.3$. The derived planet parameters are summarized in Table 6; K2-415b's mass is estimated to be $3.0 \pm 2.7 M_\oplus$ ($M_p < 7.5 M_\oplus$ at 95% confidence).

To compare K2-415b with other small planets around the lowest-mass stars, we were tempted to put K2-415b in the mass–radius diagram, although the mass constraint for the planet is rather weak. Figure 12 plots the planet masses versus
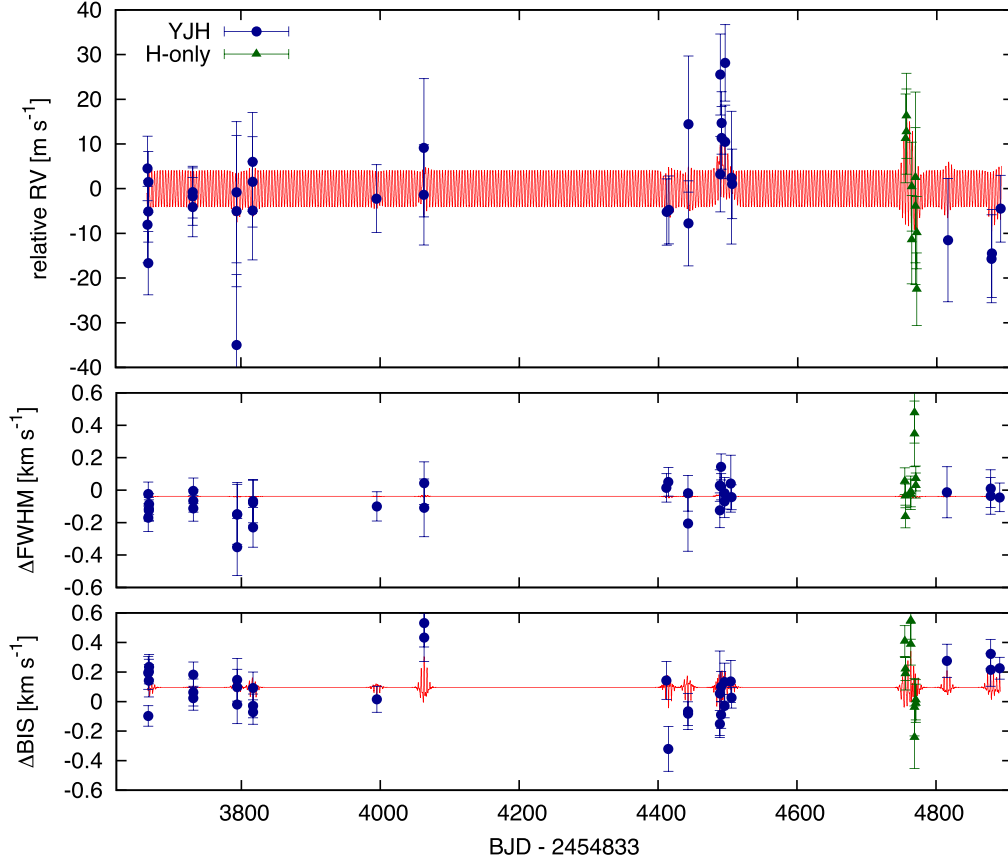
Figure 10. Observed RVs (top) as well as the activity indicators (middle and bottom panels) measured from the IRD spectra. The red solid lines indicate the multidimensional GP regressions to the observed quantities using the quasi-periodic GP kernel.
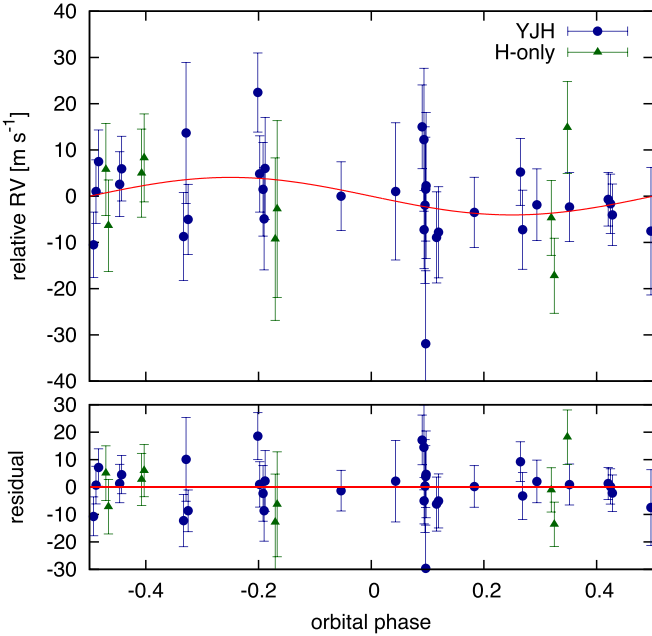

Figure 11. Phase-folded RV curve after subtracting the correlated-noise component via the GP regression. The red solid line represents the best-fit Keplerian orbit of K2-415b, and the bottom panel plots the residuals from the best-fit orbit.

Table 6
Final Planetary Parameters of K2-415b

Parameter	Value
P (days)	4.0179694 ± 0.0000027
$T_{c,0} - 2454833$ (BJD)	3267.07116 ± 0.00069
R_p ($R_\oplus$)	1.015 ± 0.051
M_p ($M_\oplus$)	3.0 ± 2.7
a (au)	0.0270 ± 0.00023
i_o (deg)	89.32 ± 0.41
S_p ($S_\oplus$)	$4.82^{+0.45}_{-0.42}$
T_{eq} ($A_B = 0$) (K)	412.4 ± 9.3
T_{eq} ($A_B = 0.3$) (K)	377.2 ± 8.6

radii for the well-characterized planets based on the TEPcat database (Southworth 2011); K2-415b and the planets around the lowest-mass stars ($<0.3\,M_\odot$) are plotted by the red square and colored circles, respectively. As expected, due to the weak constraint on the planet mass, we are unable to discuss in detail the internal structure of K2-415b at this point. Nonetheless, the planet seems to be in line with the trend of other known small planets around the lowest-mass stars, having an Earth-like composition. The expected mass for a 100% iron planet with $R_p = 1.015\,R_\oplus$ is $\approx 2.2\,M_\oplus$, which gives a theoretical upper limit on the mass of K2-415b (i.e., its true mass is likely less than this limit). It is also evident from the figure that the size of the planet is incompatible with possessing a H_2-dominated atmosphere with $T_{eq} = 400$ K. According to the recent finding by Luque & Pallé (2022) on the population of small planets around low-mass stars, a $1\,R_\oplus$ planet has to have a rocky composition, as opposed to water-rich planets having slightly larger radii ($\gtrsim 1.5\,R_\oplus$).
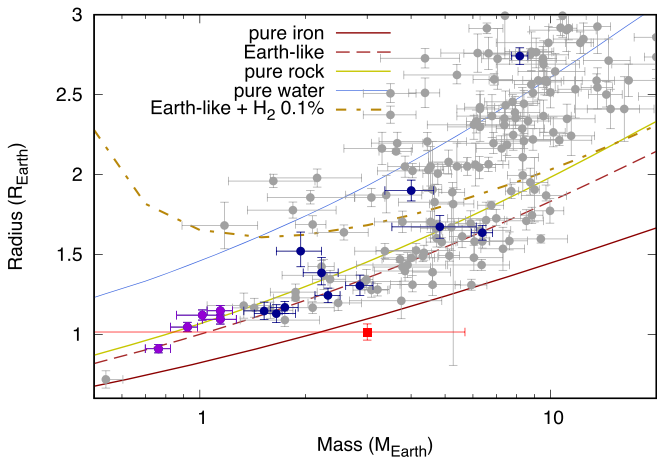
Figure 12. Mass–radius diagram for well-characterized transiting planets, taken from the TEPcat catalog (Southworth 2011). K2-415b, planets around the low-mass stars ($0.1\,M_\odot < M_\star < 0.3\,M_\odot$), and TRAPPIST-1 planets are plotted by the red square, dark blue circles, and purple circles, respectively. Theoretical curves are drawn using the models by Zeng et al. (2016, 2019), in which an equilibrium temperature of 400 K was assumed.

In theoretical aspects, recent models of planet formation via planetesimal accretion (Kimura & Ikoma 2022) predict that there exist rocky planets of ~ 0.3–$2\,M_\oplus$ with no atmosphere and no or small amounts of water around late-M dwarfs. Alternatively, in the context of the pebble accretion scenario, given that our estimated planetary mass is comparable to the pebble isolation mass (~ 1–$2\,M_\oplus$) near the snowline around low-mass stars (Liu et al. 2019, 2020), inward migration of planetary embryos with the isolation mass followed by giant impacts (e.g., Matsumoto et al. 2020) would be another possible formation pathway for K2-415b.

At 22 pc, K2-415 is currently the closest planet-hosting star from Earth identified by the Kepler/K2 missions, followed by K2-129 (27.8 pc; Dressing et al. 2017) and G 9-40 (27.9 pc; Stefansson et al. 2020). K2-415 is also one of the lowest-mass stars hosting an Earth-like planet ($R_p < 1.25\,R_\oplus$). The only M dwarfs cooler than K2-415 hosting Earth-like transiting planets are TRAPPIST-1 (12 pc; Gillon et al. 2017), LP 791-18 (26 pc; Crossfield et al. 2019), LHS 1140 (15 pc; Dittmann et al. 2017), and Kepler-42 (40 pc; Muirhead et al. 2012). Moreover, as of today, there are only ten transiting-planet (of any size) hosting stars cooler than K2-415, seven of which are more distant stars than K2-415.

Given its proximity to Earth and moderate transit depth ($\approx 0.25\%$), K2-415b could be a potential target for future atmospheric characterizations of Earth-like planets, especially those having a relatively low temperature (e.g., $T_{\rm eq} < 500$ K). To determine the prospects for atmospheric characterization, it is necessary to constrain the planet mass more precisely via further RV observations. Existing spectrographs for precision RV measurements can potentially place a good constraint on the planet mass, but with the current RV precision achieved by IRD (3–4 m s^{-1}), a huge number of RV measurements (>200) would be required. Instead, red-optical Doppler instruments such as MAROON-X (Seifahrt et al. 2020), which can achieve a better RV precision for early- to mid-M dwarfs, may be able to deliver a better constraint on K2-415b's mass with a more reasonable number of observations; for instance, according to the integration time calculator,[36] MAROON-X would be able

to achieve peak S/N ratios of 40–50 (blue arm) and ≈ 80 (red arm) with a 30 minute integration for K2-415, which translate to an RV precision of 1.2–1.3 m s^{-1}. Assuming this precision and one Earth mass for K2-415b, we simulated RV observations and analyses in order to see to what extent one can constrain the mass of the planet via MAROON-X. Because the star exhibits a moderate RV jitter, the mass constraint would ultimately rely on the degree of substantive suppression of RV jitter by post-processing (such as the GP regression above). Therefore, we simulated RV measurements with three different RV jitter magnitudes (1.0 m s^{-1}, 2.0 m s^{-1}, 5.0 m s^{-1}), which were included as additional Gaussian scatters to simulated data points.[37] As a result of simulating and analyzing 150 RV points by MAROON-X observations, we found that the planet mass ($M_p = 1.0\,M_\oplus$) is constrained with 6.2σ, 4.2σ, and 2.0σ for the assumed RV jitter values of 1.0 m s^{-1}, 2.0 m s^{-1}, and 5.0 m s^{-1}, respectively.

Once the planet mass is measured at the 4σ–5σ level, one may simulate the atmospheric characterization with space-based telescopes (e.g., JWST) and/or future 20–30 m class telescopes. Detailed simulated observations for K2-415b with existing and future facilities are beyond the scope of this paper, but we briefly mention the feasibility of JWST observations based on the atmospheric scale height of K2-415b: Assuming an Earth mass, $T_{\rm eq}$ of 377 K, and an Earth-like atmosphere (i.e., a mean molecular mass of 4.8×10^{-26} kg) for K2-415b, we obtain an expected atmospheric scale height of $H \approx 11$ km. The amplitude of spectral features in transmission spectroscopy (e.g., Equation (3) of Kreidberg 2018) is then estimated to be ≈ 16 ppm, which is comparable to the noise floor (~ 10 ppm) expected for JWST NIRSpec observations (Rustamkulov et al. 2022). Also, given the magnitudes of K2-415, it would be a challenging target to probe for an Earth-like atmosphere, even with JWST. However, this does not rule out the possibility of detecting signals for an atmosphere with a higher scale height. More detailed prospects for future atmospheric characterization, such as the transmission spectroscopy metric (TSM; Kempton et al. 2018), will be discussed once the planet mass is better-constrained by future RV monitoring.

K2-415b is located slightly inward of the classical habitable zone (Kopparapu et al. 2016) based on the insolation flux onto the planet, but an outer planet, if any, in the system with a slightly longer period (e.g., 10–15 days) could sit inside the habitable zone. Little is known on the properties of multi-planet systems around the lowest-mass stars ($<0.3\,M_\odot$), but assuming that their properties are similar to those in the "Kepler-multi" systems, the planets could have a typical spacing of ~ 20 mutual Hill radii (Weiss et al. 2018). Recently, Hoshino & Kokubo (2023) also showed that the typical orbital spacing of planets formed by giant impacts is ~ 20 mutual Hill radii, independently of stellar masses, through N-body simulations. Thus, it is quite possible that a secondary planet having $\sim 1\,M_\oplus$ has an orbital period of 10–15 days.

As noted in Section 2, the joint BLS analysis for K2 and TESS light curves resulted in a nondetection of any other transiting objects in the system. In order to see if any additional planet signals could be detected in the RV data, we ran the periodogram analysis for the IRD RVs after eliminating the

---

[37] RV jitters are correlated noise, but we assumed that correlated-noise components are more or less suppressed by post-processing and extending the temporal baseline of RV measurements. Thus, the assumed jitters here are remaining noise after their suppression.

best-fit orbit of K2-415b. The second panel from the top in Figure 9 draws the LS periodogram for the RV residuals; no significant peak is identified. The lack of TTVs and significant peaks in the BLS search (Section 2) as well as the LS periodogram suggests that K2-415b does not have a "massive" outer friend, but it does not rule out the presence of additional low-mass planets in the system. An Earth-mass planet ($M_p \sin i_o = 1.0\,M_\oplus$) with a period of 10 days would induce an RV semi-amplitude of $K = 1.0\,\mathrm{m\,s^{-1}}$, which is well below the detection limit for the IRD data, especially given that the system has relatively large RV jitters. Although it is not straightforward to detect an "Earth-mass" planet with a period of 10 days, future RV monitoring would enable us to constrain the presence of an outer planet of a few Earth masses, in addition to obtaining a better constraint on K2-415b's mass.

We note that K2-415b could also be a potential target for stellar obliquity measurement via the Rossiter–McLaughlin (RM) effect (Rossiter 1924; McLaughlin 1924). Provided that K2-415's $v \sin i$ is similar to its equatorial velocity of $\approx$2.3 km s^{-1},[38] we expect an RV anomaly semi-amplitude of 3–5 m s^{-1}. It is challenging to achieve this RV precision with IRD while obtaining a good time sampling during a transit (transit duration is only 1 hour), but again, red-optical Doppler instruments like MAROON-X may be able to detect the RM signal for K2-415b. These RM measurements would also provide observations to look for atmospheric signatures, such as in the hydrogen and metal lines.

6. Summary

Based on the analysis of K2 light curves, we detected an Earth-sized ($R_p = 1.015 \pm 0.051\,R_\oplus$) planet candidate with $P = 4.02$ days around K2-415, which is an M5 dwarf star at 22 pc. The same target was later observed by TESS, which also identified the same candidate, calling the system TOI-5557. Our follow-up observation campaign between 2018 and 2022, including IRCS AO imaging, WIYN speckle observations, and IRD near-infrared spectroscopy, allowed us to rule out FP scenarios for K2-415b and statistically validate the planet. The RV measurements by IRD were not capable of pinning down the mass of K2-415b, due to the small number of data points and relatively large RV jitters (8–10 m s^{-1}), but our careful GP modeling of the observed RVs, together with some activity indicators (ΔFWHM and ΔBIS), placed a weak constraint of $M_p = 3.0 \pm 2.7\,M_\oplus$ for the mass of the planet. The distance of 22 pc and the moderate depth of the transit make K2-415 a good target for future observations, including further RV monitoring (e.g., to search for additional planets) and transit spectroscopy.

Facilities: Subaru (IRD, IRCS), WIYN (NESSI).

Software: vespa (Morton 2015), TRICERATOPS (Giacalone et al. 2021).

ORCID iDs

Teruyuki Hirano ◉ https://orcid.org/0000-0003-3618-7535
Fei Dai ◉ https://orcid.org/0000-0002-8958-0683
John H. Livingston ◉ https://orcid.org/0000-0002-4881-3620
Sascha Grziwa ◉ https://orcid.org/0000-0003-3370-4058
Yui Kasagi ◉ https://orcid.org/0000-0002-8607-358X
Norio Narita ◉ https://orcid.org/0000-0001-8511-2981
Hiroyuki Tako Ishikawa ◉ https://orcid.org/0000-0001-6309-4380
Kohei Miyakawa ◉ https://orcid.org/0000-0002-5706-3497
Luisa M. Serrano ◉ https://orcid.org/0000-0001-9211-3691
Yuji Matsumoto ◉ https://orcid.org/0000-0002-2383-1216
Eiichiro Kokubo ◉ https://orcid.org/0000-0002-5486-7828
Tadahiro Kimura ◉ https://orcid.org/0000-0001-8477-2523
Masahiro Ikoma ◉ https://orcid.org/0000-0002-5658-5971
Joshua N. Winn ◉ https://orcid.org/0000-0002-4265-047X
John P. Wisniewski ◉ https://orcid.org/0000-0001-9209-1808
Hiroki Harakawa ◉ https://orcid.org/0000-0002-6197-5544
Huan-Yu Teng ◉ https://orcid.org/0000-0003-3860-6297
William D. Cochran ◉ https://orcid.org/0000-0001-9662-3496
Akihiko Fukui ◉ https://orcid.org/0000-0002-4909-5763
Davide Gandolfi ◉ https://orcid.org/0000-0001-8627-9628
Eike W. Guenther ◉ https://orcid.org/0000-0002-9130-6747
Yasunori Hori ◉ https://orcid.org/0000-0003-4676-0251
Kai Ikuta ◉ https://orcid.org/0000-0002-5978-057X
Kiyoe Kawauchi ◉ https://orcid.org/0000-0003-1205-5108
Emil Knudstrup ◉ https://orcid.org/0000-0001-7880-594X
Judith Korth ◉ https://orcid.org/0000-0002-0076-6239
Takayuki Kotani ◉ https://orcid.org/0000-0001-6181-3142
Vigneshwaran Krishnamurthy ◉ https://orcid.org/0000-0003-2310-9415
Tomoyuki Kudo ◉ https://orcid.org/0000-0002-9294-1793
Masayuki Kuzuhara ◉ https://orcid.org/0000-0002-4677-9182
Rafael Luque ◉ https://orcid.org/0000-0002-4671-2957
Mayuko Mori ◉ https://orcid.org/0000-0003-1368-6593

---

[38] We attempted to derive the $v \sin i$ of K2-415 from the IRD spectrum, but we were unable to constrain it because M5 stars' spectra are dominated by molecular lines, which in many parts disagree with synthetic spectra (e.g., Allard et al. 2013).

Jun Nishikawa ⓘ https://orcid.org/0000-0001-9326-8134
Masashi Omiya ⓘ https://orcid.org/0000-0002-5051-6027
Jaume Orell-Miquel ⓘ https://orcid.org/0000-0003-2066-8959
Enric Palle ⓘ https://orcid.org/0000-0003-0987-1593
Carina M. Persson ⓘ https://orcid.org/0000-0003-1257-5146
Seth Redfield ⓘ https://orcid.org/0000-0003-3786-3486
Alexis M. S. Smith ⓘ https://orcid.org/0000-0002-2386-4341
Aoi Takahashi ⓘ https://orcid.org/0000-0003-3881-3202
Vincent Van Eylen ⓘ https://orcid.org/0000-0001-5542-8870
Sébastien Vievard ⓘ https://orcid.org/0000-0003-4018-2569
Motohide Tamura ⓘ https://orcid.org/0000-0002-6510-0681
Bun'ei Sato ⓘ https://orcid.org/0000-0001-8033-5633

References

Allard, F., Homeier, D., Freytag, B., et al. 2013, MSAIS, 24, 128
Asensio Ramos, A., & Petit, P. 2015, A&A, 583, A51
Bogner, M., Stelzer, B., & Raetz, S. 2022, AN, 343, e10079
Boisse, I., Bonfils, X., & Santos, N. C. 2012, A&A, 545, A109
Brady, M. T., & Bean, J. L. 2022, AJ, 163, 255
Burn, R., Schlecker, M., Mordasini, C., et al. 2021, A&A, 656, A72
Claret, A., Hauschildt, P. H., & Witte, S. 2013, A&A, 552, A16
Crossfield, I. J. M., Waalkes, W., Newton, E. R., et al. 2019, ApJL, 883, L16
Dawson, R. I., Chiang, E., & Lee, E. J. 2015, MNRAS, 453, 1471
Desort, M., Lagrange, A. M., Galland, F., Udry, S., & Mayor, M. 2007, A&A, 473, 983
Dittmann, J. A., Irwin, J. M., Charbonneau, D., et al. 2017, Natur, 544, 333
Donati, J.-F., Semel, M., Carter, B. D., Rees, D. E., & Collier Cameron, A. 1997, MNRAS, 291, 658
Dressing, C. D., & Charbonneau, D. 2015, ApJ, 807, 45
Dressing, C. D., Vanderburg, A., Schlieder, J. E., et al. 2017, AJ, 154, 207
Elkins-Tanton, L. T., & Seager, S. 2008, ApJ, 685, 1237
Fridlund, M., Gaidos, E., Barragán, O., et al. 2017, A&A, 604, A16
Gaia Collaboration, Brown, A. G. A., Vallenari, A., et al. 2021, A&A, 649, A1
Gaidos, E., Mann, A. W., Kraus, A. L., & Ireland, M. 2016, MNRAS, 457, 2877
Gandolfi, D., Barragán, O., Hatzes, A. P., et al. 2017, AJ, 154, 123
Gardner, J. P., Mather, J. C., Clampin, M., et al. 2006, SSRv, 123, 485
Giacalone, S., Dressing, C. D., Jensen, E. L. N., et al. 2021, AJ, 161, 24
Gillon, M., Triaud, A. H. M. J., Demory, B.-O., et al. 2017, Natur, 542, 456
Girardi, L., Groenewegen, M. A. T., Hatziminaoglou, E., & da Costa, L. 2005, A&A, 436, 895
Grunblatt, S. K., Howard, A. W., & Haywood, R. D. 2015, ApJ, 808, 127
Guerrero, N. M., Seager, S., Huang, C. X., et al. 2021, ApJS, 254, 39
Harakawa, H., Takarada, T., Kasagi, Y., et al. 2022, PASJ, 74, 904
Hardegree-Ullman, K. K., Cushing, M. C., Muirhead, P. S., & Christiansen, J. L. 2019, AJ, 158, 75
Hayano, Y., Takami, H., Guyon, O., et al. 2008, Proc. SPIE, 7015, 701510
Henden, A. A., Templeton, M., Terrell, D., et al. 2016, VizieR Online Data Catalog, II/336
Hirano, T., Masuda, K., Sato, B., et al. 2015, ApJ, 799, 9
Hirano, T., Fukui, A., Mann, A. W., et al. 2016, ApJ, 820, 41
Hirano, T., Dai, F., Gandolfi, D., et al. 2018, AJ, 155, 127
Hirano, T., Kuzuhara, M., Kotani, T., et al. 2020, PASJ, 72, 93
Hirano, T., Livingston, J. H., Fukui, A., et al. 2021, AJ, 162, 161
Hoshino, H., & Kokubo, E. 2023, MNRAS, 519, 2838
Howell, S. B., Everett, M. E., Sherry, W., Horch, E., & Ciardi, D. R. 2011, AJ, 142, 19
Howell, S. B., Sobeck, C., Haas, M., et al. 2014, PASP, 126, 398
Ikoma, M., & Genda, H. 2006, ApJ, 648, 696
Ishikawa, H. T., Aoki, W., Kotani, T., et al. 2020, PASJ, 72, 102
Ishikawa, H. T., Aoki, W., Hirano, T., et al. 2022, AJ, 163, 72
Johnstone, C. P. 2020, ApJ, 890, 79
Kempton, E. M. R., Bean, J. L., Louie, D. R., et al. 2018, PASP, 130, 114401

Kimura, T., & Ikoma, M. 2022, NatAs, 6, 1296
Kite, E. S., & Schaefer, L. 2021, ApJL, 909, L22
Kobayashi, N., Tokunaga, A. T., Terada, H., et al. 2000, Proc. SPIE, 4008, 1056
Koizumi, Y., Kuzuhara, M., Omiya, M., et al. 2021, PASJ, 73, 154
Kopparapu, R. k., Wolf, E. T., Haqq-Misra, J., et al. 2016, ApJ, 819, 84
Kotani, T., Tamura, M., Nishikawa, J., et al. 2018, Proc. SPIE, 10702, 1070211
Kovács, G., Zucker, S., & Mazeh, T. 2002, A&A, 391, 369
Kreidberg, L. 2018, in in Handbook of Exoplanets, ed. H. J. Deeg & J. A. Belmonte (Cham: Springer), 100
Lammer, H., Lichtenegger, H. I. M., Kulikov, Y. N., et al. 2007, AsBio, 7, 185
Lépine, S., & Shara, M. M. 2005, AJ, 129, 1483
Lichtenberg, T., Bower, D. J., Hammond, M., et al. 2021, JGRE, 126, e06711
Liu, B., Lambrechts, M., Johansen, A., & Liu, F. 2019, A&A, 632, A7
Liu, B., Lambrechts, M., Johansen, A., Pascucci, I., & Henning, T. 2020, A&A, 638, A88
Lopez, E. D., & Fortney, J. J. 2014, ApJ, 792, 1
Luger, R., & Barnes, R. 2015, AsBio, 15, 119
Luo, A. L., Zhao, Y.-H., Zhao, G., et al. 2015, RAA, 15, 1095
Luque, R., & Pallé, E. 2022, Sci, 377, 1211
Mann, A. W., Feiden, G. A., Gaidos, E., Boyajian, T., & von Braun, K. 2015, ApJ, 804, 64
Mann, A. W., Dupuy, T., Kraus, A. L., et al. 2019, ApJ, 871, 63
Matsumoto, Y., Gu, P.-G., Kokubo, E., Oshino, S., & Omiya, M. 2020, A&A, 642, A23
Mayor, M., Marmier, M., Lovis, C., et al. 2011, arXiv:1109.2497
McLaughlin, D. B. 1924, ApJ, 60, 22
Millholland, S. C., & Spalding, C. 2020, ApJ, 905, 71
Morton, T. D. 2015, VESPA: False positive probabilities calculator, Astrophysics Source Code Library, ascl:1503.011
Morton, T. D., Bryson, S. T., Coughlin, J. L., et al. 2016, ApJ, 822, 86
Muirhead, P. S., Johnson, J. A., Apps, K., et al. 2012, ApJ, 747, 144
Ohta, Y., Taruya, A., & Suto, Y. 2009, ApJ, 690, 1
Otegi, J. F., Bouchy, F., & Helled, R. 2020, A&A, 634, A43
Owen, J. E., & Wu, Y. 2013, ApJ, 775, 105
Owen, J. E., & Wu, Y. 2017, ApJ, 847, 29
Rajpaul, V., Aigrain, S., Osborne, M. A., Reece, S., & Roberts, S. 2015, MNRAS, 452, 2269
Ramirez, R. M., & Kaltenegger, L. 2014, ApJL, 797, L25
Ricker, G. R., Winn, J. N., Vanderspek, R., et al. 2015, JATIS, 1, 014003
Rossiter, R. A. 1924, ApJ, 60, 15
Rustamkulov, Z., Sing, D. K., Liu, R., & Wang, A. 2022, ApJL, 928, L7
Sabotta, S., Schlecker, M., Chaturvedi, P., et al. 2021, A&A, 653, A114
Sanchis-Ojeda, R., Rappaport, S., Pallè, E., et al. 2015, ApJ, 812, 112
Schlichting, H. E., & Young, E. D. 2022, PSJ, 3, 127
Scott, N. J. 2019, AAS/Division for Extreme Solar Systems Abstracts, 51, 330.15
Seifahrt, A., Bean, J. L., Stürmer, J., et al. 2020, Proc. SPIE, 11447, 114471F
Serrano, L. M., Gandolfi, D., Hoyer, S., et al. 2022, A&A, 667, A1
Skrutskie, M. F., Cutri, R. M., Stiening, R., et al. 2006, AJ, 131, 1163
Smith, J. C., Stumpe, M. C., Van Cleve, J. E., et al. 2012, PASP, 124, 1000
Southworth, J. 2011, MNRAS, 417, 2166
Stassun, K. G., Oelkers, R. J., Paegert, M., et al. 2019, AJ, 158, 138
Stefansson, G., Cañas, C., Wisniewski, J., et al. 2020, AJ, 159, 100
Stumpe, M. C., Smith, J. C., Catanzarite, J. H., et al. 2014, PASP, 126, 100
Stumpe, M. C., Smith, J. C., Van Cleve, J. E., et al. 2012, PASP, 124, 985
Tamura, M., Suto, H., Nishikawa, J., et al. 2012, Proc. SPIE, 8446, 84461T
Van Eylen, V., Albrecht, S., Huang, X., et al. 2019, AJ, 157, 61
Van Eylen, V., Astudillo-Defru, N., Bonfils, X., et al. 2021, MNRAS, 507, 2154
Vanderburg, A., & Johnson, J. A. 2014, PASP, 126, 948
Weiss, L. M., Marcy, G. W., Petigura, E. A., et al. 2018, AJ, 155, 48
Winn, J. N., Sanchis-Ojeda, R., & Rappaport, S. 2018, NewAR, 83, 37
Zechmeister, M., & Kürster, M. 2009, A&A, 496, 577
Zeng, L., Sasselov, D. D., & Jacobsen, S. B. 2016, ApJ, 819, 127
Zeng, L., Jacobsen, S. B., Sasselov, D. D., et al. 2019, PNAS, 116, 9723